Research Article

Study on the Adsorption Performance and Adsorption Mechanism of Graphene Oxide by Red Sandstone in Aqueous Solution

Na Li [iD],[1] WenHao Dai,[1] HaiBo Kang,[2] Beifeng Lv,[1] Ping Jiang [iD],[1] and Wei Wang[1]

[1]*School of Civil Engineering, Shaoxing University, Shaoxing 312000, China*
[2]*School of Civil Engineering, Nanjing Tech University, College of Transportation Engineering, Nanjing 211816, China*

Correspondence should be addressed to Ping Jiang; jiangping@usx.edu.cn

In order to deal with the increasingly serious pollution of graphene oxide (GO) to the environment. In this paper, the use of red sandstone to treat GO-contaminated aqueous solution is proposed for the first time, and the adsorption capacity and adsorption mechanism of red sandstone to GO are discussed. The controlled variable method was used to explore the optimal pH, concentration, and quality of red sandstone for GO aqueous solution. The adsorption isotherm, thermodynamics, and adsorption kinetics were fitted. Adsorption characterization tests were performed using XRD, AFM, XPS, FT-IR, SAP, TEM, SAP, laser particle size analyzer, and SEM. The results show that when $T = 303$ K, the optimum adsorption condition of red sandstone for GO is pH = 4, the mass of the adsorbent is 40 mg, and when the concentration of GO is 80 mg/L, the adsorption capacity is 90 mg/g. The adsorption isotherm model fits the Langmuir model. The adsorption thermodynamic experiments and fitting results show that the reaction is endothermic. XRD and FT-IR tests showed that $CaCO_3$ in red sandstone was involved in the adsorption of GO. SEM, TEM, and AFM microscopic results showed that GO was adsorbed on the surface of red sandstone particles. The XPS test showed that Ca^{2+} in red sandstone and C=O bond in GO undergo ionic or coordination reaction. The adsorption kinetics fit a pseudo-second-order kinetic model. This study will provide some references for the removal of GO in the environment and the interaction mechanism with natural minerals.

1. Introduction

Due to the large specific surface area $(2630 \, m^2 \cdot g^{-1})$, more oxygen-containing functional groups (hydroxyl, carboxyl, epoxy groups, etc.), and excellent water dispersibility and solubility (the GO solubility in water is $0.712 \, g \cdot L^{-2}$), graphene oxide (GO) is often used to adsorb organic pollutants and inorganic pollutants such as metal ions [1, 2] or load other excellent adsorption materials such as SBA-15, MCM-41, and MCM-48, for the treatment of pollutants or the extraction of substances in aqueous solutions [3–6]. Alternatively, graphene oxide layer photocatalysts were used for visible light degradation of chloramphenicol (CMP) [7]. Some scholars have also loaded GO on CuO as a fuel additive to improve the physical and chemical properties of diesel [8], although GO has many nice features. However, some

scholars have found that GO has certain harm to the ecological environment [9–12], and its main ecological harm is mainly reflected in the following two aspects: (1) mechanical damage: due to the layered structure of GO, its edge is relatively sharp, which may damage the cell membrane and cell wall after entering cell [13]; (2) oxidative stress: after GO enters cells, due to its strong oxidative ability, oxidative stress will occur in cells, resulting in cellular lipid peroxidation and DNA damage [14]. In view of the certain ecological hazards of GO, how to deal with GO has become a hot research issue once it is leaked during transportation. Adsorption using adsorbents is an efficient, environmentally friendly, and relatively inexpensive method. Many scholars are trying to find low-cost, high-efficiency, and environmentally friendly materials. Shi et al. studied the migration behavior of GO in aqueous solution and compared the

adsorption capacity of GO by different cations and different kinds of clay minerals. The results showed that the adsorption of GO by different ions was related to water and radius of ions, and the hydroxyl and metal-oxygen bonds of clay minerals can interact with GO. Different types of clay minerals have different cohesive capacities for GO due to their different electrical properties in aqueous solutions, and their adsorption capacities are as follows: nanoalumina > kaolin > bentonite > montmorillonite [15]. Wang et al. studied the adsorption capacity of GO by different layered double hydroxides and compared the effects of different ratios of Mg/AL- and Ca/(Mg+AL)-layered double hydroxides on GO adsorption. It was found that the adsorption capacity of GO varied under different Mg/AL and Ca/(Mg+AL) ratios. When the ratio of Mg/AL was 4, the adsorption effect was the best; when the ratio of Ca/(Mg+AL) was 1, the best effect was achieved. The temperature and ions in the solution had little effect on GO adsorption [16]. Zhao et al. found that the adsorption between GO and negatively charged rocks was mainly electrostatic attraction and difficult to desorption by studying the interaction between GO and montmorillonite and kaolinite [17]. Feriancikova and Xu studied the adsorption capacity of GO by saturated sand and found that a small amount of retained particles occurred at low ionic strength (e.g., 1 mL of NaCl). When the ionic strength was raised to 100 mL of NaCl, the retention of degranulation increased significantly but was limited by its retention capacity. The Langmuir model can describe the migration behavior of saturated sand to degranulate [18]. In the study of Zhou and others, the effect of iron tailing sand on GO adsorption was investigated. The experimental data showed that pH, iron tailing quality, GO concentration, and temperature all had an effect on the removal of GO. The adsorption model conforms to the Langmuir monolayer adsorption model, and the adsorption process is a spontaneous process. Physical adsorption [19]. The removal of contaminated GO from water using calcareous sand from the South China Sea is studied by Lv et al. The experimental results show that the adsorption of GO on calcareous sand can reach the adsorption equilibrium within 5 h [20]. The above scholars have conducted in-depth research on the adsorption of GO by geotechnical minerals. Whether there are other geotechnical minerals that can react with GO needs to be further explored.

Red sandstone is a widespread rock that has been used as a building material since ancient times due to its bright colors [21]. Red sandstone is composed of feldspar, quartz, and clasts with a porous structure [22]. Many scholars have studied the properties of red sandstone [23–26] mostly on its mechanical and physical properties, but there are few studies on its adsorption properties. The natural porous structure of red sandstone has good adsorption properties. Chen et al. studied the kinetic characteristics of arsenic (V) adsorption on red soil after sandstone weathering. The results showed that chemical adsorption was the main adsorption process, and the adsorption effect was the best when pH = 7.0, $T = 293$ K, and As(V) concentration was less than 4.0 mg/L, and the hydraulic retention time was not less than 180 min [27]. Song et al. studied the adsorption kinetics and thermo-

dynamics of Ni(II) by Pisha sandstone. The results showed that the adsorption was carried out when $T = 293$ K and pH = 7, the equilibrium was reached at 30 min, and the adsorption capacity of Ni(II) was 23.688 mg/g. The adsorption process of Ni(II) by Pisha sandstone can be described by the Langmuir pseudo-second-order kinetic model, which is mainly ion exchange and chemical adsorption, while chemical precipitation plays a little role in this process [28].

In summary, although some scholars have studied the adsorption of heavy metal ions on red sandstone, few people have paid attention to the adsorption of GO on red sandstone. As a relatively cheap and easily available adsorbent, red sandstone has many characteristics of a good adsorbent, such as high adsorption capacity, large specific surface area, and large volume [29]. It has broad application prospects in adsorption. Therefore, red sandstone was designed as adsorbent to remove GO in aqueous solution, and the adsorption effect of different pH, temperature, GO concentration, adsorbent mass, and different time was studied. At the same time, laser particle size analyzer (Mastersizer3000) X-ray diffractometer (XRD), Fourier Transform Infrared Spectroscopy (FTIR), scanning electron microscopy (SEM), Atomic Force Microscopy (AFM), high-resolution transmission electron microscopy (TEM), and X-ray photoelectron spectroscopy (XPS) were used to analyze the microstructure and characterization of the adsorbed samples and reveal its adsorption mechanism.

2. Test Materials and Methods

2.1. Materials. The red sandstone used in the experiment was collected from Yueyang City, Hunan Province, China. It is brownish red with fine-grained structure and uniform texture. The main components are quartz, clasts, and feldspar. The cementation composition is mainly iron, which is a hard brittle sedimentary rock. Figure 1(a) shows the crushed red sandstone. The proportion of grain size of red sandstone is shown in Figures 1(b) and 1(c). It can be seen from the particle size distribution diagram that the proportion of powdery red sandstone with particle size less than 90 μm is 84.8%, and the particle size of powdery red sandstone is mainly concentrated between 1 μm and 100 μm, and the average particle size is 56.8 μm.

The GO aqueous solution is produced by Suzhou Tanfeng Technology Co., Ltd., with a concentration of 2 mg/mL and a specific surface area of 2630m²/g. Its chemical element composition is shown in Table 1.

2.2. Test Section

2.2.1. Test Scheme. Red sandstone powder was taken as adsorbent, and the adsorption rate of GO by red sandstone was investigated by different pH, temperature, GO concentration, and adsorbent mass. The test steps are as follows:

Crush the obtained samples and put them in an oven to continue drying for 24 hours, taking into account the effect of particle size on the adsorption capacity. This paper chose to use a standard sieve with a 0.074 mm aperture to screen
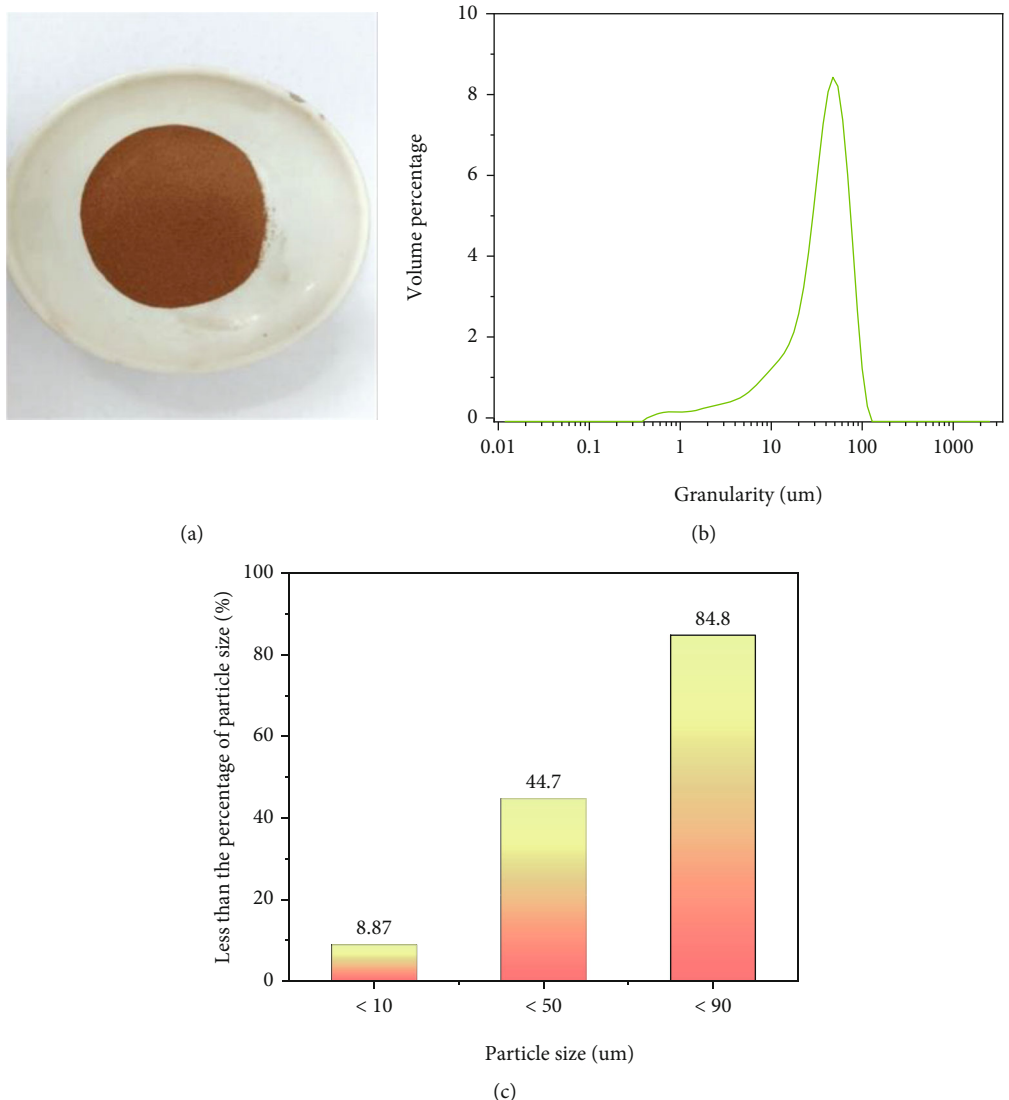
(a)

(b)

(c)

FIGURE 1: (a) Crushed red sandstone. (b) The proportion of different particle sizes of red sandstone. (c) The proportion of red sandstone smaller than a certain particle size.

TABLE 1: GO elemental composition of graphene oxide (%).

Elemental composition	C	O	H	S
Content (%)	41.70	51.49	2.41	2.00

fine particles (Figure 1). It is used to reduce the effect of particle size on adsorption [30].

When using, first sonicate the GO aqueous solution with an ultrasonic device for 30 minutes, so that it can be uniformly dispersed in the aqueous solution. Then, different volumes of GO solution and deionized water were taken with a pipette and placed in a volumetric flask, so that the total volume of GO and deionized water was 50 mL. Sodium hydroxide solution and nitric acid solution with negligible volumes were added to adjust to different pH, and then, red sandstone powder with different mass was added.

Oscillation mixing. The above-prepared solution was poured into a volumetric flask and then put into a shaker at different temperatures. After shaking for 3 h at 240 rpm, the volumetric flask was taken out and put into a constant temperature curing box to stand for 24 h at different temperatures.

Absorbance test. 1 mL of the middle-layer clear liquid after adsorption was put into a test tube, and then 24 mL of deionized water was added to make a 25 mL solution. After standing for 10 min, the absorbance was measured by an ultraviolet spectrometer (incident wavelength $\lambda = 210$ nm). The relationship between absorbance and concentration was obtained by linear regression analysis. The relationship between absorbance (y) and concentration (x) is the calibration curve. GO was selected as (0 mg/L, 1 mg/L, 2 mg/L, 3 mg/L, 4 mg/L, and 5 mg/L) solutions of 6 different concentrations, and then, the absorbance was measured with an ultraviolet/visible spectrophotometer (UV75N). The measured data can be linearly fitted and then brought into the calculation to obtain the concentration of the measured solution [31], and the average value was taken through three

time measurements. The adsorption capacity, adsorption rate, and distribution coefficient were obtained from formulas (1), (2), and (3), respectively [32].

$$R = \frac{C_0 - C_e}{C_0} \times 100\%, \qquad (1)$$

$$Q_e = \frac{C_0 - C_e}{m} \times V, \qquad (2)$$

$$K_d = \frac{C_0 - C_e}{C_0} \times \frac{V}{m}, \qquad (3)$$

where C_0 represents GO concentration (mg/L), C_e represents solution concentration at adsorption equilibrium (mg/L), Q_e represents adsorption capacity (mg/g), m represents adsorbent mass (mg), V represents solution volume (mL), and K_d is distribution coefficient.

2.2.2. Microscopic Characterization. Constant temperature shaker (THZ-100B), UV/Vis spectrophotometer (UV75N), pH meter (FE28), electronic analytical balance (FA324C), X-ray diffractometer (XRD, Empyrean), Fourier transform infrared spectrometer (FTIR, NEXUS), scanning electron microscope (SEM, JSM-6360LV), atomic force microscope (AFM, SPA400), high-resolution transmission electron microscope (TEM, JEM-2100F), X-ray photoelectron spectroscopy (XPS, Thermo ESCALAB 250XI), a specific surface area analyzer (Tristar 3020II), and a laser particle sizer (Mastersizer 3000) were used to analyze the microscopic and characterization of the adsorbed precipitate samples.

3. Results and Analysis

3.1. Morphology Analysis

3.1.1. XRD. XRD can analyze the crystal structure and material composition of red sandstone and GO as well as the adsorbed products [33]. Cu target Kα was used as the radiation power source to characterize GO, red sandstone, and GO/red sandstone derivatives by XRD, as shown in Figure 2. PDF cards refer to the ICSD standard. The characteristic peaks before and after adsorption are compared. There is an obvious (001) characteristic peak at 10.08° in the GO spectrum. In the XRD pattern of red sandstone, 20.84° and 26.26° can be marked as SiO_2 (046), 27.88° can be marked as $(Na,Ca)Al(Si,Al)_3O_8$ (041), and 29.44° can be marked as $CaCO_3$ (005) [34]. In the diffraction pattern of GO/red sandstone, the peak intensity of $CaCO_3$ (005) decreases from 18090.5 cm^{-1} to 8169.5 cm^{-1}, and that of $(Na,Ca)Al(Si,Al)_3O_8$(041) also decreases from 18801.1 cm^{-1} to 11042.4 cm^{-1}, compared with that of red sandstone. The diffraction peak of GO disappears, indicating that $CaCO_3$ and $(Na,Ca)Al(Si,Al)_3O_8$ (041) in red sandstone may be involved in the adsorption of GO, rather than the simple stacking of GO on the surface of red sandstone.

3.1.2. Brunauer-Emmett-Teller (BET) Surface Area Analysis. The specific surface area and pore size are the main factors affecting the adsorption [35], so we measured the specific
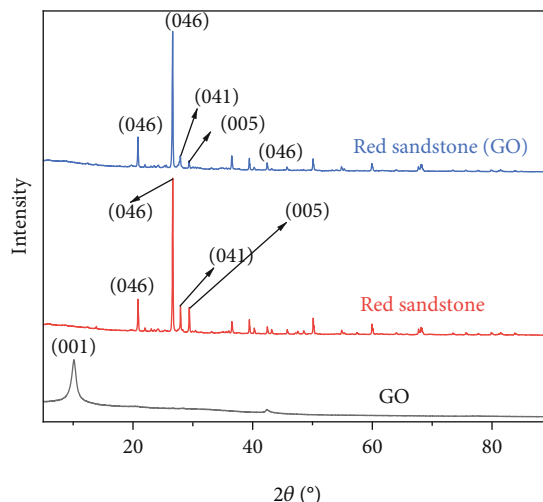

Figure 2: XRD image of GO, red sandstone, and GO/red sandstone.

Table 2: Red sandstone-specific surface area, pore size, and volume.

Material	Pore volume	BET surface	Pore size
Red sandstone	0.019024 cm^3/g	10.0729 m^2/g	56.9122 Å

surface area and pore size of the red sandstone. At the same time, in order to reduce the influence of the adsorbent moisture on the experimental results of the comparative surface area. All samples should be dried at 300°C for 3 hours and vacuumed. In the experiment, high-purity (99.99%) N_2 was used as the adsorbate, and the amount of N_2 adsorption at different relative pressures was measured in a low-temperature environment. The final measurement results are shown in Table 2: we found that the specific surface area of red sandstone is 10.0729m^2/g, which is larger. The average pore volume is 0.019024 cm^3/g, and the average pore size is 5.69122 nm. This shows that red sandstone is a natural large specific surface area and an excellent adsorbent.

3.1.3. SEM and TEM. The samples before and after adsorption were observed by scanning electron microscopy (SEM) and high-resolution transmission electron microscopy (TEM), and the obtained microscopic morphologies are shown in Figure 3 [36, 37]. Figures 2(a) and 2(b) are the SEM and TEM pictures of red sandstone, through which the sharp edges and irregular shapes of red sandstone can be clearly seen. Figures 2(c) and 2(d) are the SEM and TEM images of GO, through which we can find the multilayered two-dimensional flake-like structure of GO, with some folds on the edges and smooth in the center [38]. Figures 2(e) and 2(f) are the SEM and TEM morphology of GO/red sandstone after adsorption, and the film-like GO attached to the surface of red sandstone particles can be clearly seen.

3.1.4. FT-IR. In order to further analyze which chemical bonds in GO are involved in the adsorption, FT-IR was used
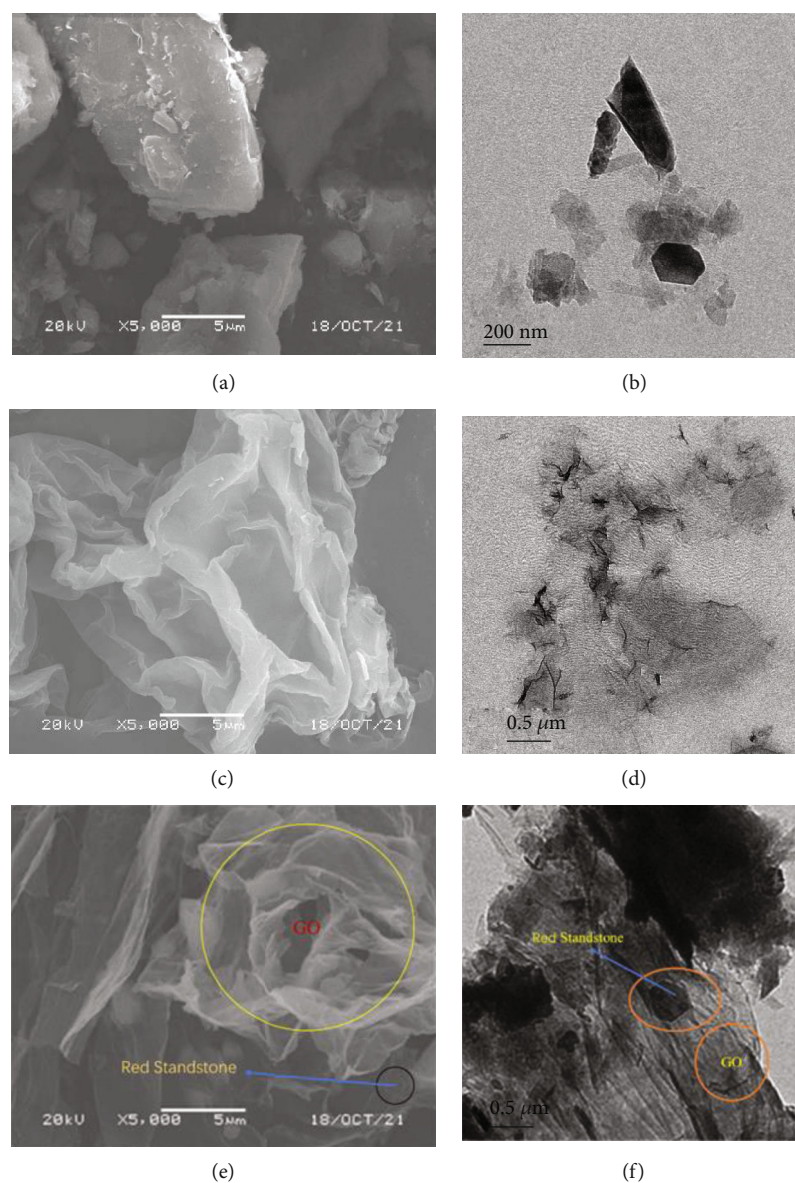
Figure 3: (a) SEM and (b) TEM of red sandstone; (c) SEM and (d) TEM of GO; (e) SEM and (f) TEM of GO/red sandstone.

to analyze the changes of functional groups and the migration and disappearance of chemical bonds of GO, red sandstone, and GO/red sandstone derivatives after adsorption [39], as shown in Figure 4. GO exhibits stretching vibration of the -OH group at 3403 cm^{-1}, stretching vibration of C=O at 1734 cm^{-1} [40], stretching vibration of C=C on the benzene ring skeleton structure at 1628 cm^{-1} [41], stretching vibration of C-OH at 1219 cm^{-1}, and vibration peak of C-O at 1049 cm^{-1} [42]. Red sandstone presents characteristic peaks of CO^3-out-of-plane deformation vibration in $CaCO_3$ at 875 cm^{-1} and 712 cm^{-1} [43], and symmetrical stretching vibration peak of Si-O bond in SiO_2 at 468 cm^{-1} [44]. The peak of GO/red sandstone weakens at 1628 cm^{-1}, disappears at 1734 cm^{-1}, 1219 cm^{-1}, 1049 cm^{-1}, 875 cm^{-1}, 712 cm^{-1}, and 590 cm^{-1}, and strengthens at 468 cm^{-1}. The disappearance of the peak at 1734 cm^{-1} may be caused by the combination of Ca^{2+} in red sandstone and O-C=O bond in GO, resulting

in the coagulation of GO [45], which is consistent with the change rule of the peak value of $CaCO_3$ in XRD pattern, indicating that GO has undergone ionic reaction or coordination reaction on the surface of red sandstone [46].

3.1.5. XPS and AFM. XPS is an effective characterization method that can qualitatively and quantitatively detect elements. Through the XPS spectra, the position of the characteristic spectral line is used to qualitatively analyze the elemental composition of material; the elemental content is quantitatively analyzed by the intensity of the photoelectron spectral line; the chemical state of each element can be further determined by peak fitting [47]. The characterization results are shown in Figure 5(a). Through the spectra, various strong peaks can be clearly seen, such as O1s, C1s of GO, O1s, C1s, Ca2p, Si2p, and Al2p of red sandstone and GO/red sandstone, which conforms to the results of XRD
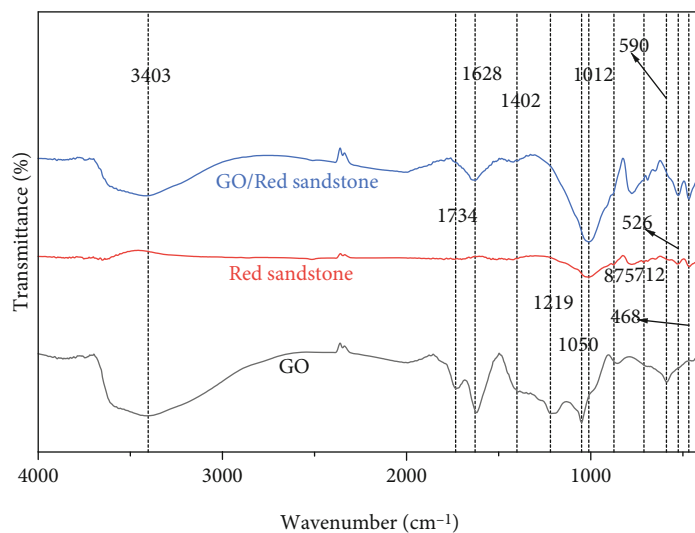
FIGURE 4: FT-IR analysis of GO, red sandstone, and GO/red sandstone.

analysis. The peak of C1s in the spectra of red sandstone is lower (7898.35), and that in the spectra of GO/red sandstone is higher (17768.9), but it is still much lower than that in the spectra of GO (30106.2). Therefore, by performing peak fitting of C1s of GO and GO/red sandstone, the C1s spectra can be deconvolved and integrated into three components at 284.8 eV, 286.2 eV, and 289.0 eV [48]. The fitting results are shown in Figures 5(b) and 5(c). It can be found through fitting that the three convolutions of C1s of GO/red sandstone had obvious changes compared with that of GO. The most obvious changes are the bonds of C-O and O-C=O, which change from 286.2 eV and 289.0 eV to 286.69 eV and 287.02 eV, respectively. The proportion of the peak area of C-O decreases from 43% to 16%, and that of O-C=O increases from 15% to 39%. From the position changes of the three convolutional components of C1s and the proportion change of the peak area before and after adsorption, it can be seen that GO has solidified on the surface of red sandstone [49], which is consistent with the results of FT-IR analysis.

AFM can further explore the height and morphology of GO and GO solidified on the surface of red sandstone [50]. The surface thicknesses of GO and GO/red sandstone were characterized, as shown in Figure 6. It can be seen from Figure 6 that GO exhibits a single-layer or double-layer structure [51], and the maximum thickness is only 2.4 nm as shown in Figures 6(a) and 6(c). For the GO/red sandstone samples, we can clearly see red sandstone particles with a height of 4.5 nm and GO attached to the surface of red sandstone particles, as shown in Figures 6(b) and 6(d), which is consistent with the results measured by SEM and TEM, indicating that GO is adsorbed on the surface of red sandstone, which further indicates that red sandstone can effectively remove GO.

3.2. The Effect of Solution pH on Adsorption. pH is an important factor affecting the interaction of substances [52]. Figure 7 shows the effect of different pH on the adsorption performance of GO by red sandstone when the adsorbent

mass is 40 mg, the solution concentration is 80 mg/L, $T = 303$ K after 24 h standing. It can be seen from the figure that with the increase of pH, the adsorption capacity of GO by red sandstone shows a trend of increasing first and then decreasing. The adsorption effect is the best when pH = 4, the adsorption rate is up to 90%, and the adsorption capacity is also 90 mg/g. The adsorption capacity at pH = 3 is smaller than that at pH = 4. Although GO itself has a certain self-coagulation capacity at acidic pH [53], its adsorption capacity is still lower than that at pH = 4, indicating that the adsorption capacity of GO by red sandstone is inhibited to a certain extent under higher acidic conditions. When pH = 4, $CaCO_3$ in red sandstone reacts with H^+ in acidic solution to form Ca^{2+}. Because GO has more oxygen-containing functional groups, it has electronegativity. Particularly, Ca^{2+} can be directly adsorbed by oxygen-containing functional groups through the double electric layer in addition to compressing the double electric layer, further neutralizing the electronegativity of GO [54]. Studies have found that metal cations are easier to combine with oxygen-containing functional groups, such as epoxy groups and carboxyl groups [55]. Therefore, when pH > 4, the adsorption capacity of GO by red sandstone gradually decreases with the increase of pH. When pH = 10, the adsorption capacity and adsorption rate are only 2.47 mg/g and 2.47%, respectively. This is because the gradual decrease of H^+ in the solution leads to the decrease of Ca^{2+}, and the gradual increase of OH^- in the solution also competes with GO for the adsorption sites on red sandstone, thereby reducing the adsorption effect.

3.3. The Effect of Adsorbent Mass on Adsorption. Figure 8 shows the effect of the red sandstone mass on the adsorption of GO. When GO concentration is 80 mg/L, pH = 4, and $T = 303$ K, the red sandstone mass is set to 10 mg, 20 mg, 30 mg, 40 mg, 50 mg, and 60 mg, respectively. After standing for 24 h, with the increase of red sandstone mass, the removal rate of GO by red sandstone shows a trend of increasing first and then decreasing. When the red
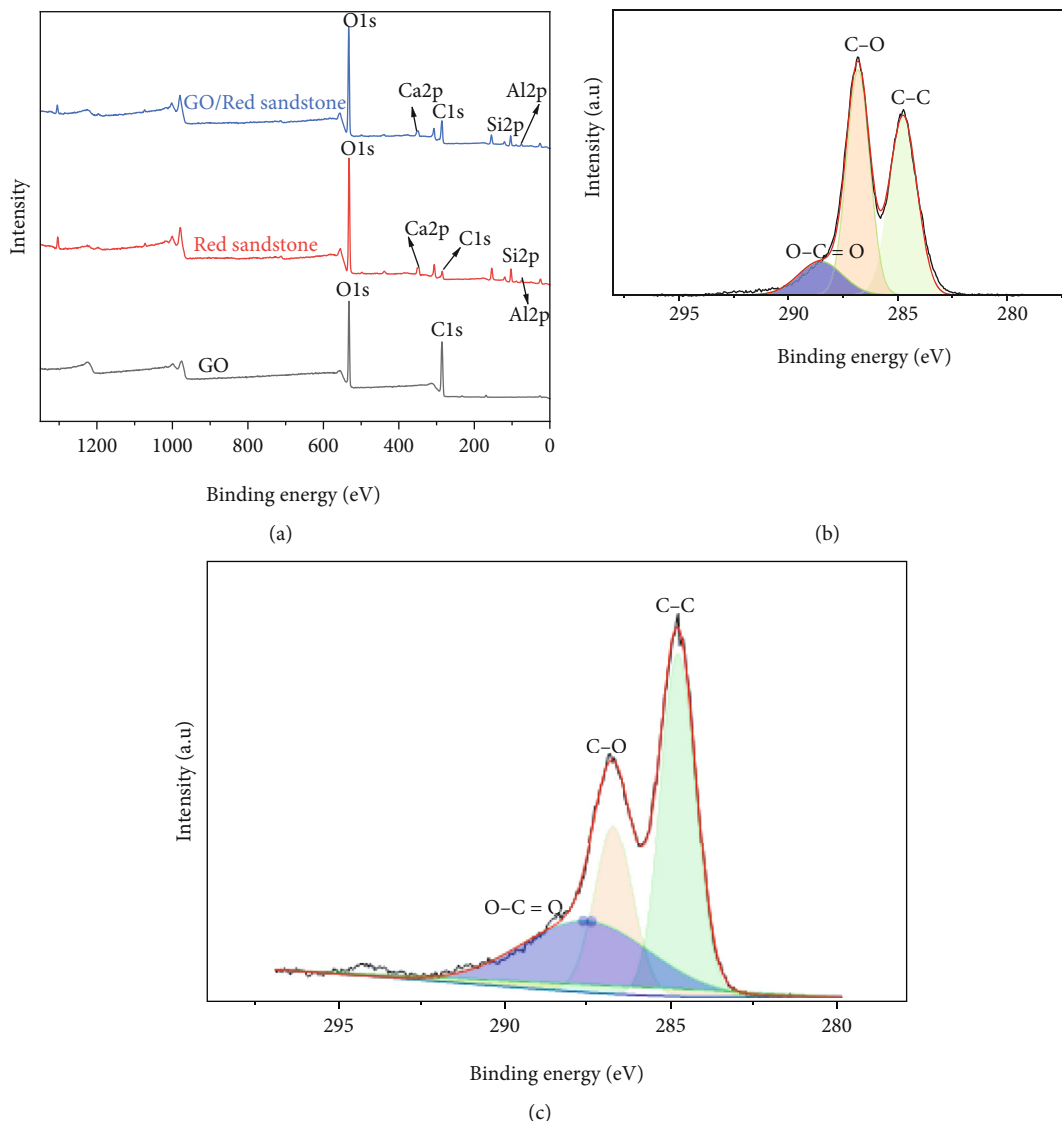
(a)

(b)

(c)

FIGURE 5: (a) XPS spectra of GO, red sandstone, and GO/red sandstone; (b) C1s XPS spectra of GO; (c) C1s XPS spectra of GO/red sandstone.

sandstone mass is 40 mg, the removal rate reaches the maximum which is 90%, and the adsorption capacity is 90 mg/g. When the red sandstone mass exceeds 40 mg, its adsorption capacity and adsorption rate decrease compared with that of 40 mg, indicating that the optimal red sandstone mass is 40 mg when GO concentration is 80 mg/L. The reason for the decrease of adsorption capacity and adsorption rate with the increase of adsorbent mass may be that with the continuous increase of red sandstone mass, red sandstone can provide more and more adsorption sites, but as GO concentration is fixed, these adsorption sites can be only combined with limited GO, resulting in an insignificant change in the late adsorption rate compared with that of red sandstone of 40 mg.

3.4. The Effect of GO Concentration on Adsorption. On the basis of the above experiments, the red sandstone mass was set to 40 mg, pH = 4, and $T = 303$ K, and the effect of GO concentration on the adsorption of GO by red sandstone

was studied after standing for 24 h. GO concentrations were set to 40 mg/L, 60 mg/L, 80 mg/L, 100 mg/L, and 120 mg/L, respectively. The test results are shown in Figure 9. It can be seen from the figure that with the continuous increase of GO concentration, the absorption capacity of GO by red sandstone generally shows a trend of first increasing and then decreasing. The best GO concentration was 80 mg/L. When the ratio of red sandstone mass to GO concentration was 0.5, the adsorption effect was the best, the adsorption capacity was 90.43 mg/g, and the distribution coefficient was 11.30. With the increase of GO concentration, the adsorption rate gradually decreased, but the adsorption capacity increased gradually. When GO concentration was 120 mg/L, the adsorption rate was only 83%, but the adsorption capacity was 125.64 mg/g, and the distribution coefficient was 6.44. It shows that the adsorption sites of red sandstone are not effectively utilized at low concentration, but with the increase of GO concentration, the adsorption sites are effectively utilized, making the adsorption capacity

0   1: Height sensor   3.6 (um)   0.0   1: Height sensor   6.2 (um)

(a)   (b)

(c)   (d)
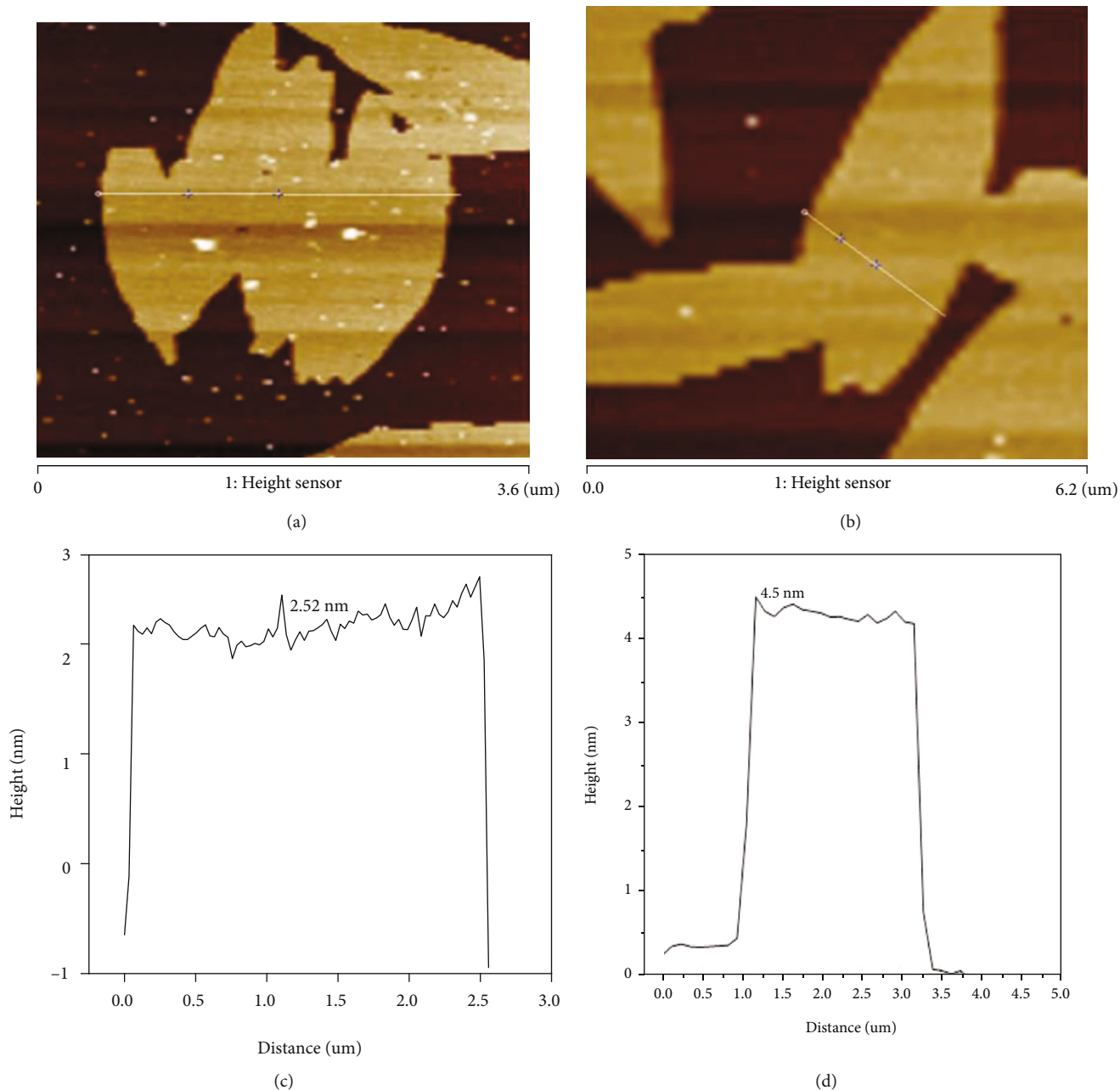
Figure 6: (a) GO AFM; (b) GO/red sandstone AFM; (c) GO height map; (d) GO/red sandstone height map.

continue to increase, but the adsorption efficiency begins to decline. The reason may be that high GO concentration makes the adsorption sites on red sandstone more easily combined with GO molecules, making it adsorb more GO. However, a certain red sandstone mass can provide a certain adsorption site, which makes the adsorption rate and distribution coefficient show a downward trend, indicating that high GO concentration has a certain inhibition effect on the adsorption capacity to a certain extent.

3.5. Adsorption Kinetics and Adsorption Thermodynamics. The above test results show that when $T = 303$ K, the optimal pH for GO adsorption by red sandstone is 4, and the optimal adsorbent mass is 40 mg. Thermodynamic experi-

ments were carried out under the optimal pH and adsorbent mass. Three temperatures (293 K, 303 K, and 313 K) and five GO concentrations (40 mg/L, 60 mg/L, 80 mg/L, 100 mg/L, and 120 mg/L) were set for thermodynamic experiments. Three control groups were set for each temperature and concentration variable. The optimal GO concentration was 80 mg/L. Therefore, the optimal pH, optimal adsorbent mass, and GO concentration were selected as the experimental conditions of adsorption kinetics.

3.5.1. Adsorption Isotherm. In nature, the temperature of an aqueous solution is different at different times. In order to explore the adsorption capacity of GO by red sandstone at different temperatures, when pH = 4, the red sandstone mass was
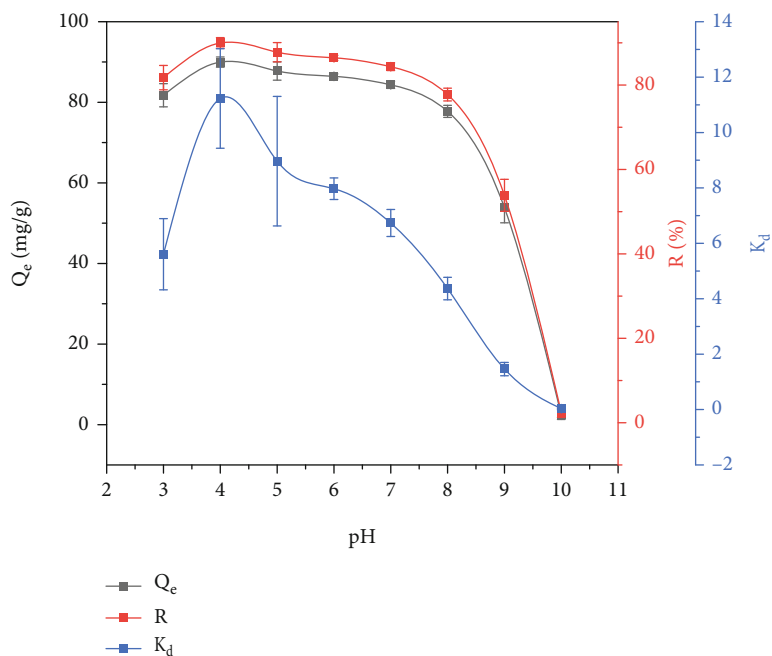
Figure 7: Effect of pH change on the adsorption of GO by red sandstone.
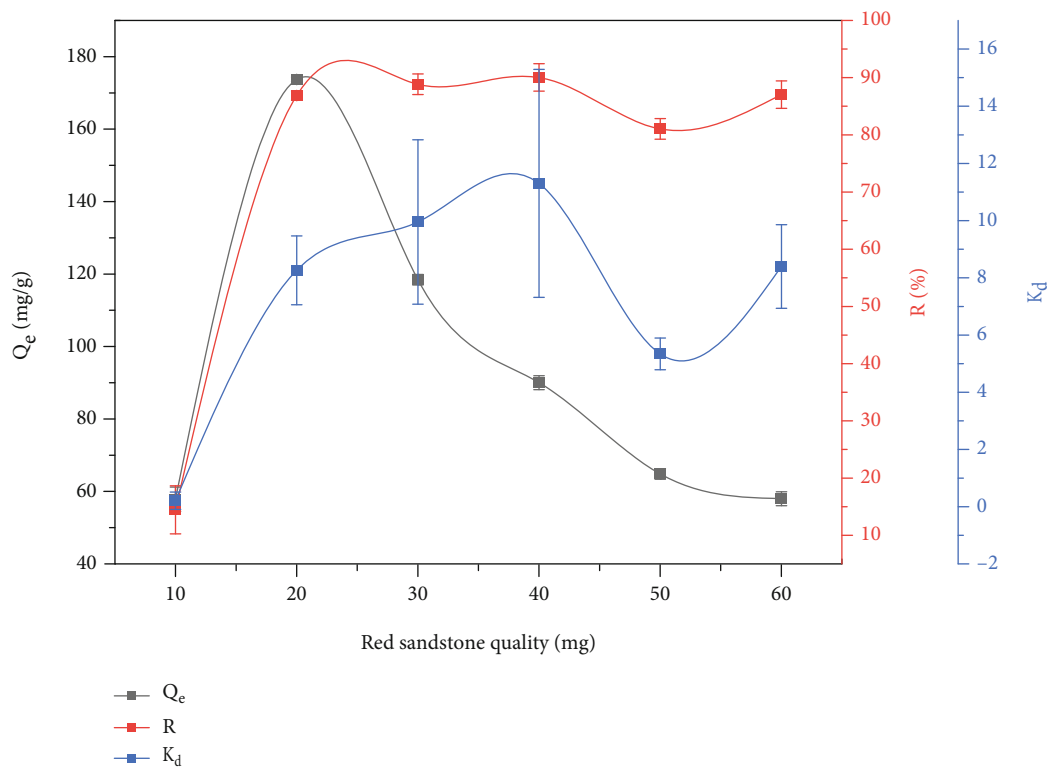

Figure 8: The effect of red sandstone mass on the adsorption of GO.

40 mg, and under three different temperatures (293 K, 303 K, and 313 K), GO solutions with different concentrations (40 mg/L, 60 mg/L, 80 mg/L, 100 mg/L, and 120 mg/L) were taken for adsorption tests. The test results are shown in Figure 10. When GO concentration is 120 mg/L, the adsorption capacity is up to 137.0 mg/g at 313 K, while that at

293 K and 303 K is only 125 mg/g and 128 mg/g, respectively. It indicates that the adsorption capacity of GO by red sandstone with the same GO concentration increases with the increase of temperature. This is because with the increase of temperature, GO molecules in the aqueous solution are more active, which greatly increases the probability of GO molecules
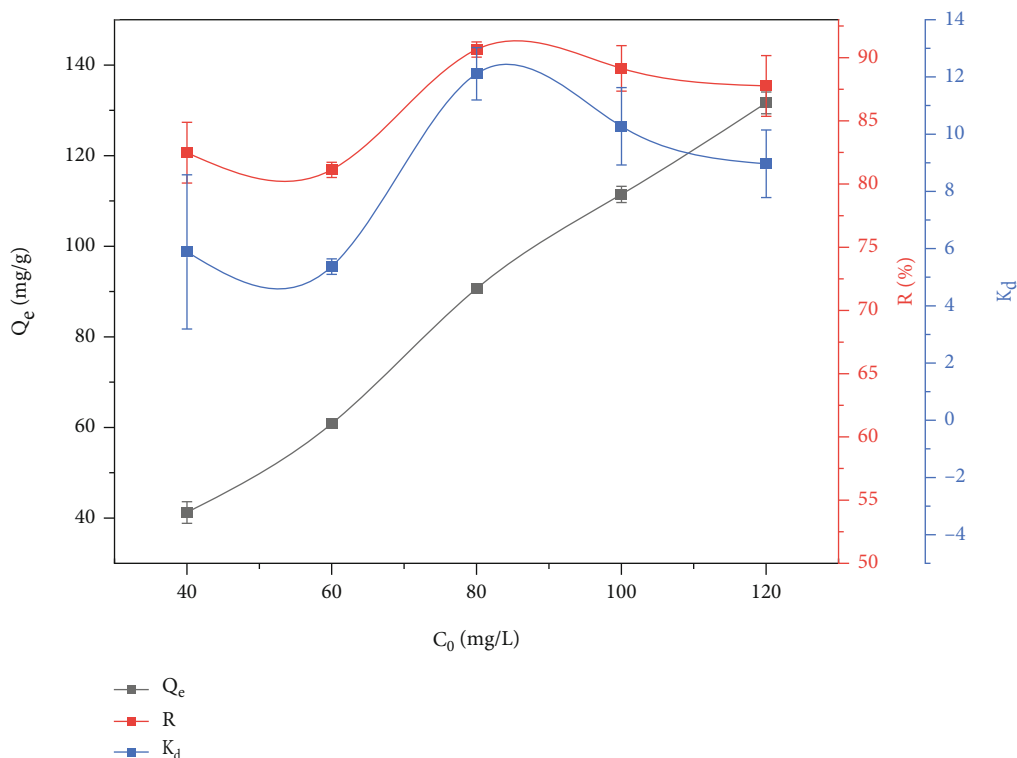
FIGURE 9: The effect of GO concentration change on the adsorption of GO by red sandstone.
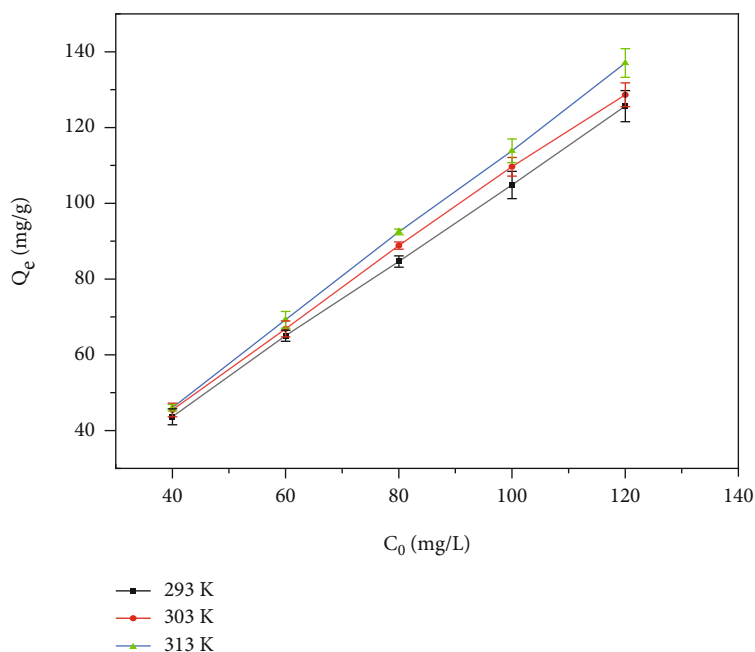

FIGURE 10: Adsorption isotherm of GO by red sandstone.

contacting the adsorption active sites on red sandstone, which leads to the increase of adsorption capacity.

In order to further explore the adsorption morphology of GO on the surface of red sandstone, Langmuir and Freundlich adsorption isotherm equations were used to fit the adsorption process, as shown in formulas (4) and (5) [56].

The fitted image is shown in Figure 11, and the fitting results are shown in Table 3. The correlation coefficients R^2 of the fitting results by the Langmuir equation are higher than those by Freundlich. It can be seen that the Langmuir equation can more accurately describe the adsorption process of GO by red sandstone, which is mainly based on
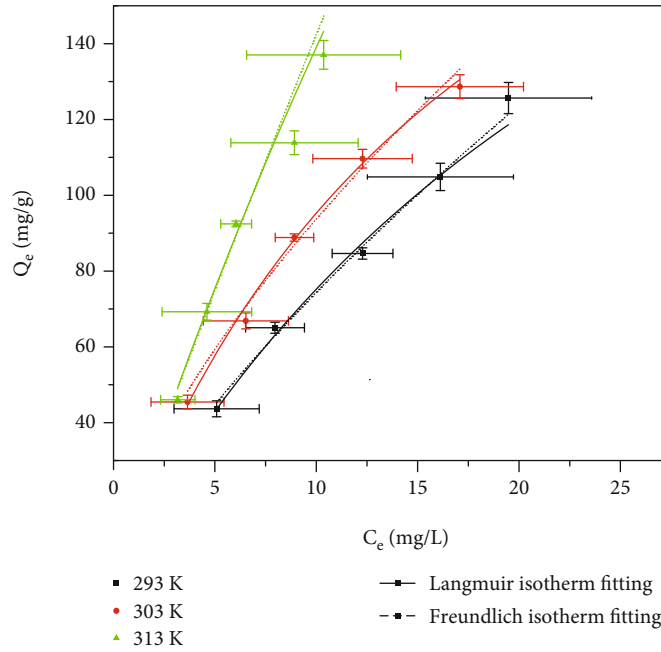
FIGURE 11: Adsorption isotherm fitting.

uniform monolayer adsorption [57]. GO attached to the surface of red sandstone can be clearly seen from the SEM and TEM images in Figures 3(e) and 2(f). The maximum adsorption capacity Q_{max} in the fitting results of the Langmuir equation increases with the increase of temperature, indicating that the increase of temperature promotes the adsorption reaction.

$$\text{Langmuir Isothermal Adsorption Model}: Q_e = \frac{bQ_{max}C_e}{1 + bC_e}, \tag{4}$$

$$\text{Freundlich Isothermal Adsorption Model}: \ln Q_e = \ln K_F + \frac{\ln C_e}{n}, \tag{5}$$

where Q_e (mg/g) represents the adsorption capacity at equilibrium; C_e (mg/L) represents the concentration of residual adsorbent in the solution after adsorption; Q_{max} (mg/g) represents the saturated adsorption capacity obtained from the fitting results; b is the adsorption equilibrium constant. K_F and n are the Freundlich adsorption equilibrium constants.

3.5.2. Adsorption Thermodynamics. In order to analyze the effect of temperature change on the adsorption of GO by red sandstone, the experimental results were calculated by fitting the thermodynamic parameters, and the energy changes during the adsorption process were analyzed to determine whether the adsorption was a spontaneous reaction or a nonspontaneous reaction [58].

Thermodynamic parameters such as standard free energy (ΔG^0), enthalpy change (ΔH^0), and entropy change (ΔS^0) were calculated by formulas (6), (7), and (8), and

the effect of temperature changes on the adsorption process was analyzed. Table 4 and Figure 12 shows the thermodynamic fitting curves and calculation parameters. At 293 K, 303 K, and 313 K, the standard free energy (ΔG^0) of GO adsorption experiments by red sandstone with different GO concentrations are all negative, indicating that the adsorption process is spontaneous. With the same GO concentration, the absolute value of standard free energy (ΔG^0) increases with the increase of temperature, indicating that the increase of temperature is beneficial to the adsorption test. However, both ΔH^0 and ΔS^0 are positive, indicating that the reaction is an endothermic reaction [59]. There are two reasons: (1) the first reason may be that with the increase of temperature, the diffusion rate of GO increases and the contact rate with minerals increases [60]; (2) the increase of temperature is conducive to the formation of chemical bonds generated, which is beneficial for chemisorption.

$$\ln K_d = \frac{\Delta S^0}{R} - \frac{\Delta S^0}{RT}, \tag{6}$$

$$\Delta G^0 = \Delta H - T\Delta S^0, \tag{7}$$

$$K_d = \frac{C_0 - C_e}{C_0} \times \frac{V}{m}, \tag{8}$$

where K_d is the distribution coefficient; R is the standard molar gas constant (8.3145 J/mol^{-1}·K^{-1}); T (K) is the absolute temperature of Kelvin.

3.5.3. Adsorption Kinetics. The adsorption rate is an important index to evaluate the adsorption performance, which

TABLE 3: Isotherm pseudo parameters.

pH	Temperature (K)	Langmuir			Freundlich		
		Q_m (mg/g)	K_l (L/mg)	R^2	K_F (mg/g)	n	R^2
	293 K	293	0.0179	0.979	21.99	1.096	0.956
4	303 K	354	0.034	0.976	16.05	1.34	0.959
	313 K	559	0.030	0.997	12.67	1.27	0.983

TABLE 4: Thermodynamic fitting parameter table.

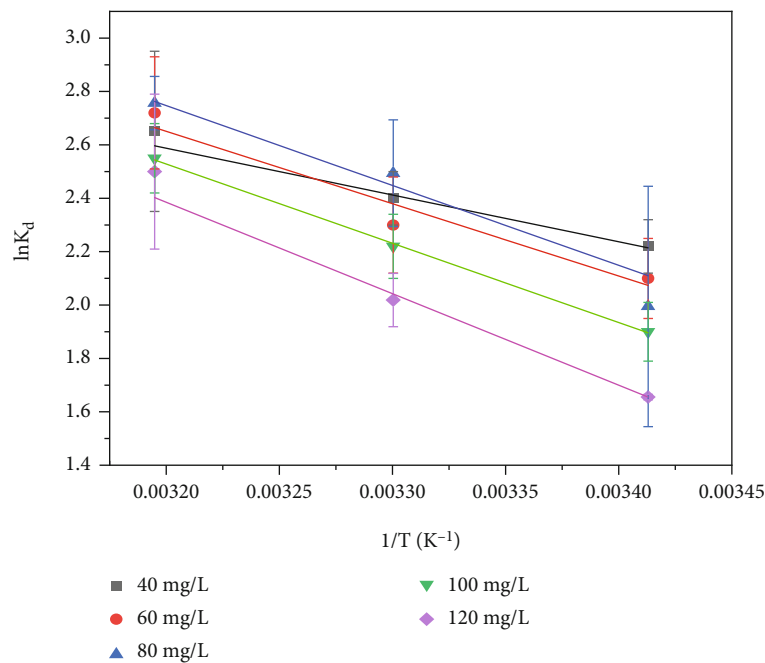| C_0 (mg/L)	ΔG^0 (kJ·mol^{-1})			ΔH^0 (kJ·mol^{-1})	ΔS^0 (J·mol^{-1}·K^{-1})
	293 K	303 K	313 K		
40	-4.35	-5.43	-6.51	27.18	107.66
60	-4.52	-5.55	-6.58	25.65	103.01
80	-4.65	-5.85	-7.04	30.34	119.47
100	-4.96	-5.92	-6.88	23.12	95.86
120	-5.10	-5.96	-6.81	19.96	85.55

FIGURE 12: Thermodynamic fitting diagram of GO adsorption by red sandstone.

is generally studied by adsorption kinetics. Adsorption kinetics can reveal the diffusion mechanism, adsorption steps, and controlling factors of adsorption [61]. At the same time, it can also reveal the time when the adsorbent reaches the adsorption equilibrium. In order to explore the above factors, the pseudo-first-order kinetic model and pseudo-second-order kinetic model are usually adopted [62], as follows:

$$\text{pseudo-first-order kinetic equation} : \ln\ (Q_e - Q_t) = \ln Q_e - k_1 t, \tag{9}$$

$$\text{pseudo-second-order kinetic equation} : \frac{t}{Q_t} = \frac{t}{Q_e} + \frac{1}{k_2 Q_e 2}, \tag{10}$$

where Q_e represents the adsorption capacity at equilibrium, mg/g; Q_t represents the adsorption capacity at time t, mg/g; k_1 and k_2 are constants, g/(mg·min); t represents the adsorption time, min.

In order to reduce the change of the solution during the sampling process, thereby increasing the concentration of GO and causing experimental errors, we set up six groups of parallel samples to sequentially extract the solution in
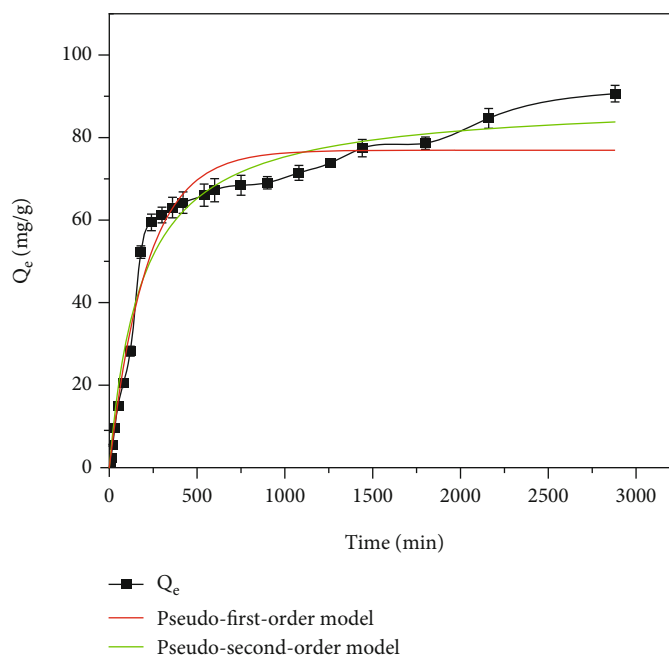
FIGURE 13: Graph of adsorption capacity over time and fitting curve of the pseudo-first-order model and pseudo-second-order model.

TABLE 5: Kinetic fit data plot.

pH	Temperature (K)	Pseudo-first-order model			Pseudo-second-order model		
		Q_e (mg/g)	k_1 g/(mg·min)	R^2	Q_e (mg/g)	k_2 g/(mg·min)	R^2
4	303 K	76.2	0.047	0.969	89.88	0.004	0.976

each time period. After solution extraction, centrifuge the extracted solution [63]. Figure 13 shows the change of adsorption capacity over time, when GO concentration is 80 mg/L, $T = 303$ K, and pH = 4, and the red sandstone mass is 40 mg. It can be seen from Figure 13 that the adsorption rate gradually decreases over time, the adsorption equilibrium is reached at 2800 min, and the adsorption capacity is 90.03 mg/g. This is mainly because the number of effective adsorption sites on the surface of red sandstone particles is relatively fixed. As the reaction time increases, there are not enough active sites on the surface of red sandstone particles for adsorption, resulting in a gradual decrease in the adsorption rate.

At the same time, the test data were fitted by kinetic formulas (9) and (10). The fitting results are shown in Figure 13 and Table 5. It can be seen from the figure that the equilibrium adsorption capacity fitted by the pseudo-first-order kinetic model is 76.2 mg/g, while that fitted by the pseudo-second-order kinetic model is 89.88 mg/g, which is closer to the actual measured data of 90.03 mg/g. In addition, the correlation coefficients R^2 of the pseudo-first-order and pseudo-second-order kinetic equations are 0.969 and 0.976, respectively. Therefore, the pseudo-second-order kinetic model equation is more suitable for describing the adsorption process of GO by red sandstone, indicating that the adsorption process belongs to chemical adsorption [64].

4. Conclusion

Red sandstone, GO, and GO/red sandstone were characterized by microscopic tests such as SEM, TEM, XPS, FT-IR, AFM, BET, and XRD, and the adsorption isotherm, adsorption thermodynamics, and adsorption kinetic models were combined to systematically reveal the adsorption mechanism of GO by red sandstone. The following main conclusions are drawn:

(1) The experimental results show that the red sandstone has a good adsorption capacity for GO. $T = 303$ K, GO concentration 80 mg/L, pH = 4, red sandstone mass 40 mg, and equilibration time 24 h. The adsorption effect is the best. The adsorption rate was 89.08%, the adsorption capacity was 89.08 g/mg, and the partition coefficient was 11.22. The adsorption of GO on red sandstone is mainly due to the coordination reaction of Ca^{2+} dissolved in the solution with C-O and O-C=O bonds, which makes GO condense on the surface of red sandstone

(2) The adsorption of GO on red sandstone conforms to the Langmuir model and belongs to monolayer adsorption. The adsorption of GO to red sandstone is endothermic, and the amount of adsorption increases with increasing temperature. The adsorption of GO on red sandstone is more in line with

the pseudo-second-order kinetic equation, which belongs to chemical adsorption. Kinetic experiments show that the adsorption equilibrium time of red sandstone is 2800 min

(3) This study did not discuss the pore size, specific surface area, and polarity of red sandstone for the adsorption capacity of GO. We will continue to explore in the next exploration

The results of this study contribute to a better understanding of the adsorption behavior of GO with natural materials in aqueous environment, which is crucial for handling GO in aqueous solution and reducing the hazard of GO in nature.

Data Availability

The data used to support the findings of this study are available from the corresponding author upon request.

Conflicts of Interest

The authors declare that there is no conflict of interest regarding the publication of this paper.

Acknowledgments

References

[1] J. Song, Y. X. Zeng, Y. Y. Liu, and W. Jiang, "Retention of graphene oxide and reduced graphene oxide in porous media: diffusion-attachment, interception-attachment and straining," *Journal of Hazardous Materials*, vol. 431, p. 128635, 2022.

[2] K. Balasubramani, N. Sivarajasekar, and M. Naushad, "Effective adsorption of antidiabetic pharmaceutical (metformin) from aqueous medium using graphene oxide nanoparticles: equilibrium and statistical modelling," *Journal of Molecular Liquids*, vol. 301, p. 112426, 2020.

[3] S. O. Akpotu, I. A. Lawal, B. Moodley, and A. E. Ofomaja, "Covalently linked graphene oxide/reduced graphene oxide-methoxylether polyethylene glycol functionalised silica for scavenging of estrogen: adsorption performance and mechanism," *Chemosphere*, vol. 246, 2020.

[4] F. Subhan, S. Aslam, Z. F. Yan et al., "Highly dispersive lanthanum oxide fabricated in confined space of SBA-15 for adsorptive desulfurization," *Chemical Engineering Journal*, vol. 384, 2020.

[5] W. M. Song, X. Liu, T. Jing, and Q. J. Deng, "Characterization and Catalytic Properties of Al-MCM-41 Mesoporous Materials Grafted with Tributyltin Chloride," *Chinese Journal of Chemical Engineering*, vol. 20, pp. 900–905, 2012.

[6] R. Zare-Dorabei, M. S. Darbandsari, A. Moghimi, M. S. Tehrani, and S. Nazerdeylami, "Synthesis, characterization and application of cyclam-modified magnetic SBA-15 as a novel sorbent and its optimization by central composite design for

adsorption and determination of trace amounts of lead ions," *RSC Advances*, vol. 6, no. 110, pp. 108477–108487, 2016.

[7] A. Kumar, A. Kumari, G. Sharma, B. Du, M. Naushad, and F. J. Stadler, "Carbon quantum dots and reduced graphene oxide modified self-assembled $_3$N$_4$/$_3$N$_4$ metal-free nano- photocatalyst for high performance degradation of chloramphenicol," *Journal of Molecular Liquids*, vol. 300, p. 112356, 2020.

[8] S. Sehar, F. Sher, S. F. Zhang, U. Khalid, J. Sulejmanovic, and E. C. Lima, "Thermodynamic and kinetic study of synthesised graphene oxide-CuO nanocomposites: a way forward to fuel additive and photocatalytic potentials," *Journal of Molecular Liquids*, vol. 313, p. 113494, 2020.

[9] R. Martin-Folgar, A. Esteban-Arranz, V. Negri, and M. Morales, "Toxicological effects of three different types of highly pure graphene oxide in the midge _Chironomus riparius_," *Science of the Total Environment*, vol. 815, p. 152465, 2022.

[10] Z. Mohammadpour, S. Ghasemzadeh, E. Askari, and F. M. Jebeli, "Iron oxychloride/bovine serum albumin nanosheets for catalytic H$_2$O$_2$ activation," *Colloids and Surfaces a-Physicochemical and Engineering Aspects*, vol. 624, 2021.

[11] C. Q. Bi, M. Junaid, Y. Liu et al., "Graphene oxide chronic exposure enhanced perfluorooctane sulfonate mediated toxicity through oxidative stress generation in freshwater clam _Corbicula fluminea_," *Chemosphere*, vol. 297, p. 134242, 2022.

[12] Z. R. Wu, B. Chan, J. Low, J. J. H. Chu, H. W. D. Hey, and A. Tay, "Microbial resistance to nanotechnologies: an important but understudied consideration using antimicrobial nanotechnologies in orthopaedic implants," *Bioactive Materials*, vol. 16, no. 16, pp. 249–270, 2022.

[13] P. Kuropka, M. Dobrzynski, B. Bazanow et al., "A study of the impact of graphene oxide on viral infection related to A549 and TC28a2 human cell lines," *Materials*, vol. 14, no. 24, p. 7788, 2021.

[14] M. Wierzbicki, A. Hotowy, M. Kutwin et al., "Graphene oxide scaffold stimulates differentiation and proangiogenic activities of myogenic progenitor cells," *International Journal of Molecular Sciences*, vol. 21, no. 11, p. 4173, 2020.

[15] L. Shi, H. Pang, X. Wang, P. Zhang, and S. Yu, "Study on the migration and transformation mechanism of graphene oxide in aqueous solutions," *Acta Chimica Sinica*, vol. 77, no. 11, pp. 1177–1183, 2019.

[16] J. Wang, X. Wang, L. Tan et al., "Performances and mechanisms of Mg/Al and Ca/Al layered double hydroxides for graphene oxide removal from aqueous solution," *Chemical Engineering Journal*, vol. 297, pp. 106–115, 2016.

[17] J. Zhao, F. Liu, Z. Wang, X. Cao, and B. Xing, "Heteroaggregation of graphene oxide with minerals in aqueous phase," *Environmental Science & Technology: ES&T*, vol. 49, no. 5, pp. 2849–2857, 2015.

[18] L. Feriancikova and S. Xu, "Deposition and remobilization of graphene oxide within saturated sand packs," *Journal of Hazardous Materials*, vol. 235, pp. 194–200, 2012.

[19] J. W. Zhou, L. M. Yao, Y. F. Wang, W. Q. Zhao, and J. H. Gu, "Study on the adsorption properties of iron tailings for GO," *Coatings*, vol. 11, no. 7, p. 768, 2021.

[20] B. Lv, W. Yu, J. Luo, B. Qian, M. B. Asefa, and N. Li, "Study on the adsorption mechanism of graphene oxide by calcareous sand in South China Sea," *Adsorption Science & Technology*, vol. 2021, article 2227570, pp. 1–15, 2021.

[21] Z. Dong, Q. Sun, J. Ye, and W. Zhang, "Changes in color and roughness of red sandstone at high temperatures," *Bulletin of Engineering Geology and the Environment*, vol. 79, no. 4, pp. 1959–1966, 2020.

[22] J. F. Zou, Y. M. Sheng, and Z. Q. Xia, "Dynamic stress properties of dynamic compaction (DC) in a red-sandstone soil-rock mixture embankment," *Environmental Earth Sciences*, vol. 76, 2017.

[23] J. Yu, S.-j. Chen, X. Chen, Y.-z. Zhang, and Y.-y. Cai, "Experimental investigation on mechanical properties and permeability evolution of red sandstone after heat treatments," *Journal of Zhejiang University-Science A (Applied Physics & Engineering)*, vol. 16, no. 9, pp. 749–759, 2015.

[24] C. Yang, S. Liu, J. Liu, H. Yang, and J. Xie, "Characteristics of self-potential of coal samples under uniaxial compression," *Journal of Applied Geophysics*, vol. 168, no. C, pp. 1–11, 2019.

[25] H. Zhang, Q. Sun, H. Jia, Z. Dong, and T. Luo, "Effects of high-temperature thermal treatment on the porosity of red sandstone: an NMR analysis," *Acta Geophysica*, vol. 69, no. 1, pp. 113–124, 2021.

[26] C. Yu, S. Tang, D. Duan et al., "The effect of water on the creep behavior of red sandstone," *Engineering Geology*, vol. 253, pp. 64–74, 2019.

[27] H. Chen, L. Liu, R. Gong, R. Wei, Q. Yi, and A. Qiu, "Comparison of kinetics of arsenic (V) adsorption on two types of red soil weathered from granite and sandstone," *Water, air and soil pollution*, vol. 227, no. 11, 2016.

[28] F. M. Song, H. G. Ge, J. Shi, Z. F. Liu, C. Li, and B. Tang, "RETRACTED ARTICLE: Adsorption kinetics and thermodynamics of Ni (II) by Pisha sandstone," *Journal of nanoparticle research: An interdisciplinary forum for nanoscale science and technology*, vol. 22, no. 7, 2020.

[29] K. R. Kalash and T. M. Albayati, "Remediation of oil refinery wastewater implementing functionalized mesoporous materials MCM-41 in batch and continuous adsorption process," *Desalination and Water Treatment*, vol. 220, pp. 130–141, 2021.

[30] H. F. Alazzawi, I. K. Salih, and T. M. Albayati, "Drug delivery of amoxicillin molecule as a suggested treatment for covid-19 implementing functionalized mesoporous SBA-15 with aminopropyl groups," *Drug Delivery*, vol. 28, no. 1, pp. 856–864, 2021.

[31] Y. A. Abd Al-Khodor and T. M. Albayati, "Employing sodium hydroxide in desulfurization of the actual heavy crude oil: theoretical optimization and experimental evaluation," *Process Safety and Environmental Protection*, vol. 136, no. 136, pp. 334–342, 2020.

[32] J. Liu, J. Zhang, L. Xing et al., "Magnetic Fe_3O_4/attapulgite hybrids for Cd(II) adsorption: performance, mechanism and recovery," *Journal of Hazardous Materials*, vol. 412, p. 125237, 2021.

[33] S. N. Ehrlich, J. C. Hanson, A. Lopez Camara et al., "Combined XRD and XAS," *Nuclear Instruments and Methods in Physics Research Section A: Accelerators, Spectrometers, Detectors and Associated Equipment*, vol. 649, no. 1, pp. 213–215, 2011.

[34] X. Y. He, T. Zhang, Y. Q. Niu et al., "Impact of catalytic hydrothermal treatment and Ca/Al-modified hydrochar on lability, sorption, and speciation of phosphorus in swine manure: microscopic and spectroscopic investigations," *Environmental Pollution*, vol. 299, p. 118877, 2022.

[35] N. A. Atiyah, T. M. Albayati, and M. A. Atiya, "Interaction behavior of curcumin encapsulated onto functionalized SBA-15 as an efficient carrier and release in drug delivery," *Journal of Molecular Structure*, vol. 1260, article 132879, 2022.

[36] L. Liberman, O. Kleinerman, I. Davidovich, and Y. Talmon, "Micrograph contrast in low-voltage SEM and cryo-SEM," *Ultramicroscopy*, vol. 218, p. 113085, 2020.

[37] O. Dieste, T. Wiss, J. C. Griveau, R. J. Konings, G. van der Laan, and R. Caciuffo, "TEM-EELS analyses of protactinium," *Materials Research Express*, vol. 6, no. 2, 2018.

[38] C. Lee, X. Wei, J. W. Kysar, and J. Hone, "Measurement of the elastic properties and intrinsic strength of monolayer graphene," *Science*, vol. 321, no. 5887, pp. 385–388, 2008.

[39] K. Dragcevic and M. Lovrecek, "Corrosion Investigation Of Printing Machines By Ft-Ir Spectroscopy," *Tehnicki Vjesnik-Technical Gazette*, vol. 19, pp. 899–906, 2012.

[40] N. A. Atiyah, T. M. Albayati, and M. A. Atiya, "Functionalization of mesoporous MCM-41 for the delivery of curcumin as an anti-inflammatory therapy," *Advanced Powder Technology*, vol. 33, no. 2, p. 103417, 2022.

[41] W. E. Gang, G. Zheng-ye, G. Shui-shui, G. Shan-yi, K. Fu-you, and X. Hong-yao, "Determination of the oxidizability on the surface of the graphene oxide layer by infrared spectroscopy," *Spectroscopy and Spectral Analysis*, vol. 40, no. 6, pp. 1722–1727, 2020.

[42] M. Acik, G. Lee, C. Mattevi et al., "The role of oxygen during thermal reduction of graphene oxide studied by infrared absorption spectroscopy," *The Journal of Physical Chemistry C*, vol. 115, no. 40, pp. 19761–19781, 2011.

[43] W. Xiang, G. Zhang, Y. Zhang, D. Tang, and J. Wang, "Synthesis and characterization of cotton-like Ca-Al-La composite as an adsorbent for fluoride removal," *Chemical Engineering Journal*, vol. 250, pp. 423–430, 2014.

[44] P. Schmidt, L. Bellot-Gurlet, V. Leá, and P. Sciau, "Moganite detection in silica rocks using Raman and infrared spectroscopy," *European Journal of Mineralogy*, vol. 25, no. 5, pp. 797–805, 2014.

[45] I. Chowdhury, N. D. Mansukhani, L. M. Guiney, M. C. Hersam, and D. Bouchard, "Aggregation and stability of reduced graphene oxide: complex roles of divalent cations, pH, and natural organic matter," *Environmental Science & Technology: ES&T*, vol. 49, no. 18, pp. 10886–10893, 2015.

[46] W. M. Algothmi, N. M. Bandaru, Y. Yu, J. G. Shapter, and A. V. Ellis, "Alginate-graphene oxide hybrid gel beads: an efficient copper adsorbent material," *Journal of Colloid & Interface Science*, vol. 397, no. Complete, pp. 32–38, 2013.

[47] D. J. Morgan, "Imaging XPS for industrial applications," *Journal of Electron Spectroscopy and Related Phenomena*, vol. 231, pp. 109–117, 2019.

[48] T. Wen, X. Wu, X. Tan, X. Wang, and A. Xu, "One-pot synthesis of water-swellable Mg-Al layered double hydroxides and graphene oxide nanocomposites for efficient removal of As(V) from aqueous solutions," *ACS Applied Materials & Interfaces*, vol. 5, no. 8, pp. 3304–3311, 2013.

[49] Y. Zou, X. Wang, Y. Ai et al., "Coagulation behavior of graphene oxide on nanocrystallined Mg/Al layered double hydroxides: batch experimental and theoretical calculation study," *Environmental Science & Technology: ES&T*, vol. 50, no. 7, pp. 3658–3667, 2016.

[50] F. Gołek, P. Mazur, Z. Ryszka, and S. Zuber, "AFM image artifacts," *Applied Surface Science: A Journal Devoted to the*

Properties of Interfaces in Relation to the Synthesis and Behaviour of Materials, vol. 304, pp. 11–19, 2014.

[51] X. Liu, X. Xu, J. Sun et al., "Interaction between Al$_2$O$_3$ and different sizes of GO in aqueous environment," *Environmental Pollution*, vol. 243, pp. 1802–1809, 2018.

[52] X. Q. Zuo, W. Chen, A. Yu, M. Le Xu, J. Cai, and Y.-X. Chen, "pH effect on acetate adsorption at Pt (111) electrode," *Electrochemistry Communications*, vol. 89, pp. 6–9, 2018.

[53] C.-J. Shih, S. Lin, R. Sharma, M. S. Strano, and D. Blankschtein, "Understanding the pH-dependent behavior of graphene oxide aqueous solutions: a comparative experimental and molecular dynamics simulation study," *Langmuir: The ACS Journal of Surfaces and Colloids*, vol. 28, no. 1, pp. 235–241, 2012.

[54] M. Izadifar, J. S. Dolado, P. Thissen, and A. Ayuela, "Interactions between Reduced Graphene Oxide with Monomers of (Calcium) Silicate Hydrates: A First- Principles Study," *Nanomaterials*, vol. 11, 2021.

[55] D. Chen, H. Feng, and J. Li, "Graphene oxide: preparation, functionalization, and electrochemical applications," *Chemical Reviews*, vol. 112, no. 11, pp. 6027–6053, 2012.

[56] J. Wang and B. Chen, "Adsorption and coadsorption of organic pollutants and a heavy metal by graphene oxide and reduced graphene materials," *Chemical Engineering Journal*, vol. 281, pp. 379–388, 2015.

[57] M. Sabzi, A. H. Jozani, F. Zeidvandi, M. Sadeghi, and S. M. Dezfuli, "Effect of 2-mercaptobenzothiazole concentration on sour-corrosion behavior of API X60 pipeline steel: electrochemical parameters and adsorption mechanism," *International Journal of Minerals, Metallurgy and Materials*, vol. 1, no. 1, pp. 271–282, 2022.

[58] Z. Fang, H. Suhua, L. Xu et al., "Adsorption kinetics and Thermodynamics of rare earth on Montmorillonite modified by sulfuric acid," *Colloids and Surfaces a-Physicochemical and Engineering Aspects*, vol. 627, 2021.

[59] S. Azizian, "Kinetic models of sorption: a theoretical analysis," *Journal of Colloid and Interface Science*, vol. 276, no. 1, pp. 47–52, 2004.

[60] X. Guo, C. Yang, Z. Dang, Q. Zhang, Y. Li, and Q. Meng, "Sorption thermodynamics and kinetics properties of tylosin and sulfamethazine on goethite," *Chemical Engineering Journal*, vol. 223, pp. 59–67, 2013.

[61] S. T. Kadhum, G. Y. Alkindi, and T. M. Albayati, "Determination of chemical oxygen demand for phenolic compounds from oil refinery wastewater implementing different methods," *Desalination and Water Treatment*, vol. 231, pp. 44–53, 2021.

[62] E. H. Khader, T. J. Mohammed, and T. M. Albayati, "Comparative performance between rice husk and granular activated carbon for the removal of azo tartrazine dye from aqueous solution," *Desalination and Water Treatment*, vol. 229, pp. 372–383, 2021.

[63] A. T. Khadim, T. M. Albayati, and N. M. Cata Saady, "Desulfurization of actual diesel fuel onto modified mesoporous material Co/MCM-41," *Environmental Nanotechnology, Monitoring & Management*, vol. 17, article 100635, 2022.

[64] L. Wang, M. Zhang, Q. Huang, C. Zhao, K. Luo, and M. Lei, "Fabrication of ACF/GO/PEI composite for adsorption of methyl orange from aqueous solution," *Journal of Nanoscience and Nanotechnology*, vol. 18, no. 3, pp. 1747–1756, 2018.